Time-domain integration of broadband terahertz pulses in a tapered two-wire waveguide

Giacomo Balistreri, Alessandro Tomasino, Junliang Dong, Aycan Yurtsever, Salvatore Stivala, José Azaña, Roberto Morandotti**

Dr. Giacomo Balistreri, Dr. Alessandro Tomasino, Dr. Junliang Dong, Prof. José Azaña, Prof. Aycan Yurtsever, Prof. Roberto Morandotti
INRS-EMT, 1650 Boulevard Lionel-Boulet, Varennes, Québec, J3X 1S2, Canada
E-mail: alessandro.tomasino@emt.inrs.ca, morandotti@emt.inrs.ca

Dr. Giacomo Balistreri, Prof. Salvatore Stivala
DEIM, University of Palermo, Viale delle Scienze, Palermo, 90128, Italy

Prof. Roberto Morandotti
University of Electronic Science and Technology of China, 610054, Sichuan, China

Keywords: THz radiation, THz waveguides, All-optical signal processing, Nonlinear optics, Ultrafast optics

In this work, we report on the time-domain integration of broadband terahertz (THz) pulses via a tapered two-wire waveguide (TTWWG). Such a guiding structure consists of two metallic wires separated by a variable air gap that shrinks down to a sub-wavelength size as we move from the waveguide input to its output. We show that while an input THz pulse propagates towards the sub-wavelength output gap, it is reshaped into its first-order time integral waveform. In order to prove the TTWWG time integration functionality, we detected the THz pulse directly within the output gap of the waveguide, so as to prevent the out-coupling diffraction from altering the shape of the time-integrated THz transient. Since the time-domain integration is due to the tight geometrical confinement of the THz radiation in a sub-wavelength gap volume, the TTWWG operational spectral range can be easily tuned by judiciously changing both the output gap size and the tapering angle. Our results lead to the physical realization of a broadband, analog THz time integrator device, which we envisioned to serve as a key building block for the implementation of complex and ultrahigh-speed analog signal processing operations in THz communication systems.

1. Introduction

Terahertz (THz) technology has been witnessing a massive growth over the past decades.[1–4] Indeed, THz radiation - electromagnetic waves with a spectral content conventionally falling in the 0.1-10x10^{12} Hz range[5] - has been proven useful in many scientific and technology fields, spanning from time-domain spectroscopy[6–8] through biomedical imaging[9–12] and quality control[13,14], to telecommunications[15–17]. Specifically, the rapidly increasing demand for higher bandwidths and data rates in wireless communication systems has inspired several groups worldwide to employ THz waves as a means to transmit and receive information.[18] Besides their high carrier frequencies that allow for the allocation of more information in a single channel, THz communication links show some crucial advantages over the current radio-frequency (RF) networks, such as a higher beam directionality and increased tolerance to scintillation effects.[19] In order to accommodate the capacity for very high data-rate transfers (> 0.1 Tb/s), it is necessary to design a series of fundamental blocks. Different types of THz devices, capable of efficiently performing analog functionalities, i.e., manipulating time-varying signals, have been extensively investigated, such as tunable spectral filters,[20–23] modulators,[24–26] as well as frequency synthesizers.[27,28] However, we still observe a significant lack of operating devices capable of manipulating wideband THz pulses, i.e., with full-width-half-maximum (FWHM) bandwidths (Δf_{THz}) a few THz-wide. This device shortage may be ascribed to the unusual nature of THz pulses, such as those generated via optical down-conversion methods. Indeed, this type of pulses generally feature single or quasi-single cycle transients, the spectra of which have carrier frequencies (f_{THz}) comparable or lower in value than their linewidths ($\Delta f_{THz} > f_{THz}$).[29–32] This condition makes conventional configurations commonly employed in optical schemes (such as the use of fiber Bragg gratings[33–36]) of rather difficult implementation in the design of similar devices for broadband THz radiation. Therefore, the realization of THz devices with relatively wide spectral response remains a challenge. An early work from Filin *et al.*[37] has dealt with the broadband time-domain differentiation of THz pulses, achieved through a standalone sub-wavelength metallic grating

operating in a transmission geometry. Additionally, a more recent work has showed that the phase-modulation induced by a piezoelectric micromachined device onto a THz pulse could lead to its time differentiation.[38] We note that, in both cases, the sub-wavelength feature of the employed devices is the key aspect allowing for a broadband operation. Nevertheless, such solutions have been implemented in a free space configuration, which makes difficult the realization of full, compact and portable THz systems. A potential way to solve this issue is through the use of THz waveguides, which confine the THz radiation and constrain the propagation within a volume size generally comparable with its central wavelength. This leads to simpler and more efficient schemes for the handling of broadband THz pulses. Specifically, parallel plate (PPWG) and two-wire (TWWG) waveguides, have been demonstrated to enable the low-loss propagation of broadband THz pulses,[39–41] without introducing a significant dispersion over a relatively long travel distance. Since both PPWGs and TWWGs feature a double-connected cross section (axial symmetry),[42] the propagation of THz radiation is supported by a transverse electromagnetic (TEM) mode. This implies a significantly high coupling efficiency with THz pulses naturally emitted by most of the available THz sources.[43] Previous works have presented signal-processing operations via the use of either a PPWG or a TWWG, such as passive notch filters,[22,44–46] with extinction ratios of several tens of decibels. In this paper, we demonstrate the time-domain integration of broadband THz pulses achieved via the use of a tailored TWWG. To do so, we take advantage of the sub-wavelength confinement experienced by a THz pulse while propagating along a tapered two-wire waveguide (TTWWG). We show that the first-order time-domain integration of the input THz waveform can be achieved over a very wide spectral window, potentially extending over the entire THz range. The implementation of a time integrator represents a fundamental unit for the realization of advanced signal processing and computing sub-systems. For instance, THz temporal integrators may be utilized for the realization of emphasis/de-emphasis communication protocols, involving a suitable signal-conditioning of broadband THz pulses in

order to improve the overall signal-to-noise ratio, in a similar way to current RF solutions.[47] Moreover, time-domain integrators represent fundamental building blocks in analog computing systems aiming at solving ordinary differential equations.[48]

2. Theoretical Aspects

In the frequency domain, an ideal system component performing the first-order time integration of an input signal $E_{IN}(f)$, provides an output signal $E_{OUT}(f)$, which satisfies the following relation:[49]

$$H(f) = \frac{E_{OUT}(f)}{E_{IN}(f)} \propto \frac{1}{j2\pi f} \quad (1)$$

In Equation 1, $H(f)$ represents the ideal transfer function of a first-order time integrator. It states that an integrator device features a purely imaginary transmission function, the magnitude of which shows a hyperbolic dependence upon the frequency. We note that the time integration enhances the lower part of the spectrum, since the hyperbolic function more effectively emphasizes the low-frequency components. Interestingly, this type of frequency behavior resembles the non-resonant enhancement of THz radiation induced by a sub-wavelength metallic slit, realized as a nano-gap in between two planar, ultra-thin metal pads.[50–52] In that configuration, the extremely reduced width of the slit causes a very tight confinement of the THz radiation within the cavity, the effectiveness of which is inversely proportional to the THz frequency. Similarly, when the THz radiation is being focused at the input of a TWWG to excite its fundamental TEM mode, the propagating THz electric field remains mostly confined in the gap between the wires. As the air gap approaches a sub-wavelength size, it is expected that the TWWG frequency behavior will also follow a trend similar to Equation 1. In order to derive the spectral response of a standard TWWG featuring a sub-λ gap, we carried out modal simulations aiming at retrieving the corresponding fundamental mode. In particular, **Figure 1**a and 1b depict the electric field distribution of the TEM eigenmode and its transverse profile on

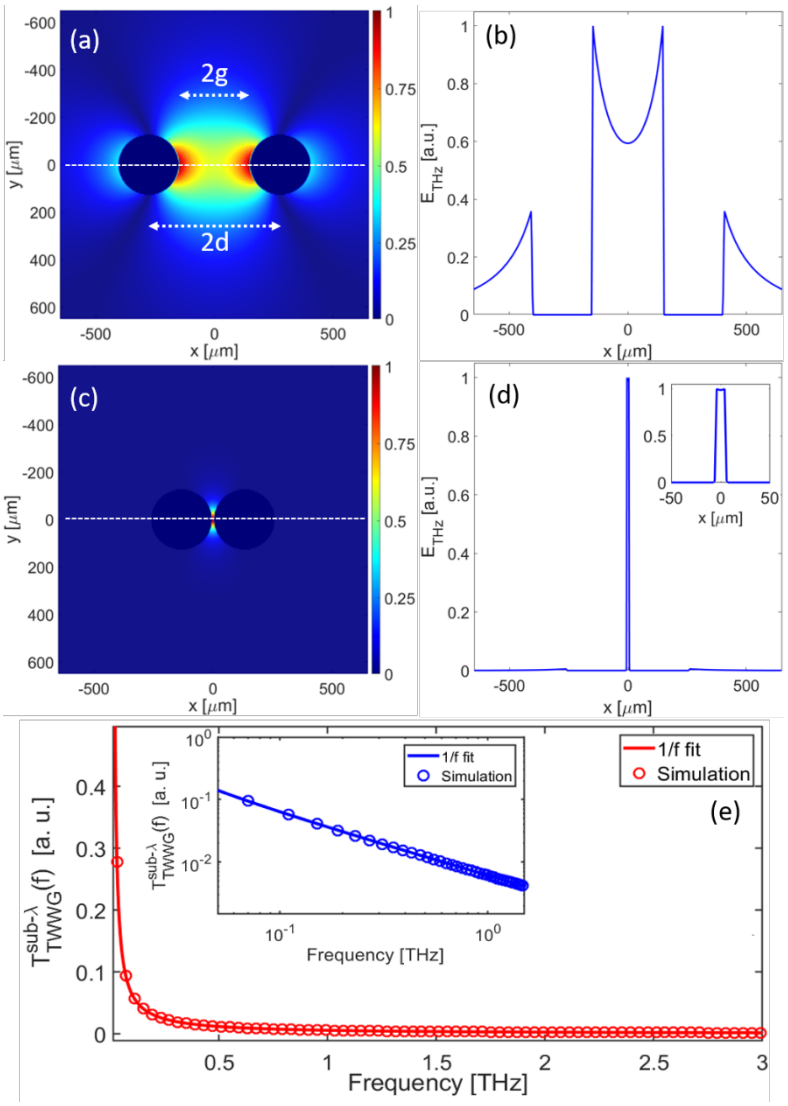

Figure 1. 2D colormap depicting the THz electric field distribution of the propagating TEM mode and its transverse profile calculated on the line crossing the wire centers (white dashed line), for the case of a TWWG with (a-b) gap of $2g = 300$ μm and (c-d) $2g = 10$ μm, respectively, assuming a propagating frequency of $f_c = 1$ THz. In both cases, the wire radius is $R = 127$ μm. The inset in (d) shows a zoom of the electric field profile in the sub-λ gap. (e) Spectral transmission of a sub-λ TWWG, as defined in Equation 2. The red solid line is a *1/f*-fitting curve. The inset shows the transmission function (blue line and dots) over a logarithmic scale.

the plane containing the wire centers, respectively. Simulations were performed for the case of two identical copper wires with a radius of $R = 127$ μm and separated by an air gap $2g = 300$ μm, at a frequency of $f_c = 1$ THz. The obtained results show that the THz electric field exhibits two identical maxima, very close to the wire surface facing the gap, yet featuring two external evanescent tails. However, as the gap shrinks down to 10 μm only, for fixed R and f_c, the field distribution shows the merging of the two maxima and the formation of a plateau over the entire

gap, as depicted in Figure 1c and 1d. Such a field profile, along with the dramatic decrease of the evanescent tails, indicates a tight confinement induced by the sub-λ gap. A detailed study about the sub-λ TWWG spectral behavior as a function of the geometrical parameters, is presented in the Supporting Informtation. Such an investigation shows that the enhancement of the THz electric field is higher when the gap and wire sizes are smaller than the THz wavelength. Here, we report the main result of these simulations in Figure 1e, which shows the spectral response $T_{TWWG}^{sub-\lambda}(f)$ of a TWWG with a 10-μm-gap, calculated as the ratio between the spectrum of the THz electric field coupled in the TWWG, $E_{TWWG}(f)$, and the spectrum of the THz electric field freely propagating in air $E_{air}(f)$. The simulated spectral response can be very well fitted with a *1/f* curve, leading to the conclusion that for a TWWG with $2g << (R, \lambda)$:

$$\left|T_{TWWG}^{sub-\lambda}(f)\right| = \left|\frac{E_{TWWG}(f)}{E_{air}(f)}\right| \propto \frac{1}{f} \quad (2)$$

According to Equation 2, it is expected that a sub-λ TWWG can perform the time integration of an input THz pulse. However, such a tightly reduced gap size causes a significant worsening of the coupling efficiency of the THz wave inside a straight TWWG, thus making its use of limited application. A way to overcome this issue is to employ a tapered structure, with a gap much wider at the input than at the output. We refer to this V-shaped geometry as a tapered-TWWG (or TTWWG), as it is schematically represented in **Figure 2**. By considering the theory of the transmission lines applied to the twin wires configuration with a variable gap along the propagation direction z, it turns out that the capacitance $C_{TTWWG}(z)$, the inductance $L_{TTWWG}(z)$ and the characteristic impedance $Z_{TTWWG}(z)$, per unit of length, can be analytically determined for high frequencies as:[43]

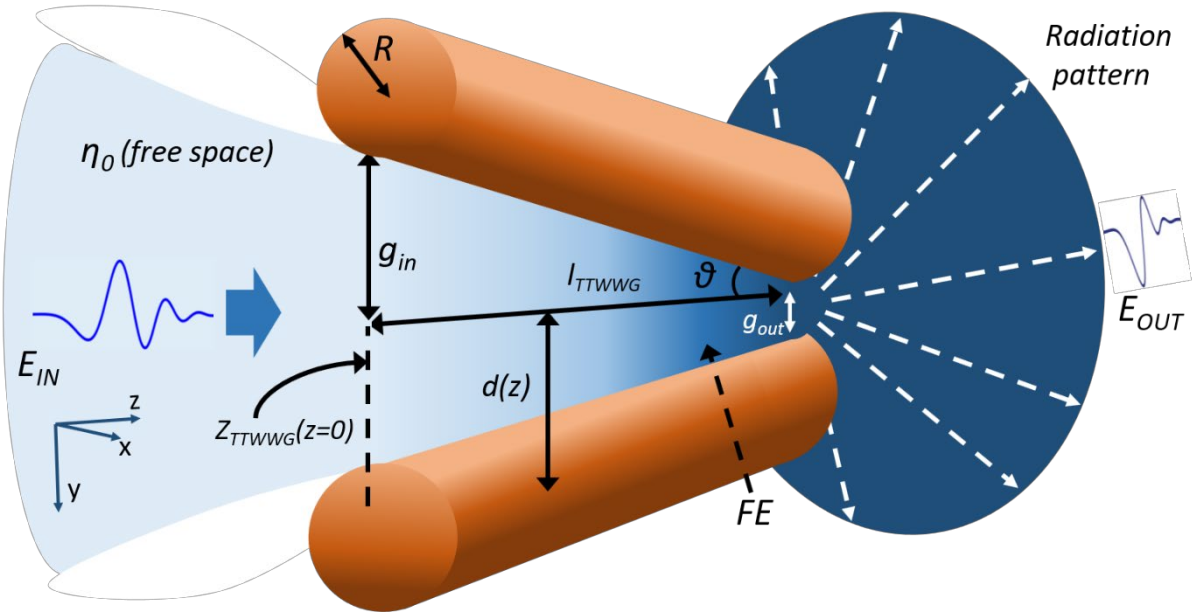

Figure 2. Schematics of the TTWWG geometry. The THz beam is focused onto the relatively large input gap (g_{in}), which improves the impedance matching between free-space (η_0) and the waveguide input [$Z_{TTWWG}(z=0)$]. While propagating towards the TTWWG output (g_{out}), the THz electric field waveform experiences a significant field enhancement (FE) induced by the geometrical confinement in an ever-decreasing gap. The THz beam is then irradiated outside the TTWWG, with an extremely large emission angle according to Bethe's diffraction.

$$C_{TTWWG}(z) = \frac{\pi\epsilon_0}{cosh^{-1}\left(\frac{d(z)}{R}\right)} \tag{3}$$

$$L_{TTWWG}(z) = \frac{\mu_0}{\pi} cosh^{-1}\left(\frac{d(z)}{R}\right) \tag{4}$$

$$Z_{TTWWG}(z) = \sqrt{\frac{L_{TTWWG}}{C_{TTWWG}}} = \frac{\eta_0}{\pi} cosh^{-1}\left(\frac{d(z)}{R}\right) \tag{5}$$

where, $d(z) = R + g(z)$ is the semi-distance between the two wire centers (see illustration in Figure 2), $cosh^{-1}$ is the inverse function of the hyperbolic cosine, ε_0, μ_0 and $\eta_0^2 = \mu_0/\varepsilon_0$ are the dielectric permittivity, magnetic permeability, and vacuum impedance, respectively. Equations (3) and (4) unveil that for gap sizes approaching the complete closure of the wire interspace, i.e., for $g \to 0$ (implying $d/R \to 1$), the TTWWG impedance tends to assume a purely capacitive nature ($C_{TTWWG} \to \infty$, $L_{TTWWG} \to 0$), as it occurs in time integrator electronic circuits.[47] In addition, Equation 5 can be exploited to design the aperture angle $\theta \approx tan^{-1}(g_{in}/L)$ of the waveguide and, in turn, the input gap $2g_{in}$, in order to tune the characteristic impedance seen from the TTWWG input end. This allows us to achieve a better impedance matching between

free-space ($\eta_0 \approx 377\ \Omega$) and waveguide, thus improving the input coupling efficiency, while also maintaining lower losses for relatively long propagation (some centimeters), compared to a straight sub-λ TWWG.[53]

3. TTWWG Characterization

For the physical demonstration of the integration functionality, we fabricated a prototype of TTWWG following a technique similar to Ref [22].[22] In particular, we used two plastic holders placed at both ends of the TTWWG support base, each one provided with a hole in the center of different diameter. Such apertures serve to fix the two gap sizes at the input and output, and to keep the wires in tension. This way, the gap size automatically narrows along the waveguide length according to a linear dependence upon the longitudinal coordinate z. Due to some fabrication limitations, the minimum diameter for the hole that could be realized was around 530 μm, thus resulting in an output gap size of roughly $2g_{out} = 24$ μm for $R = 127$ μm. The wire radius was chosen among commercially available sizes, in order to satisfy a trade-off between its robustness (to withstand the applied tension) and malleability (to be easily bent across the holder hole). The input gap size was fixed at $2g_{in} = 1100$ μm, in order to ensure that a typically tightly focused THz spot size ($w_{THz} \sim \lambda_{THz}$) could greatly overlap the TTWWG input. This also implies that most of the THz power could be coupled into the fundamental mode, being at the input $Z_{TTWWG}(z = 0) \approx 0.75\eta_0$. The total length was $l_{TTWWG} = 85$ mm, which corresponds to a tapering angle of $\theta \approx 0.36°$. A detailed investigation of the dependence of the TTWWG performance upon both the wire interspacing and radius is presented in the Supporting Information (Figure S3 and S4, respectively). A non-trivial issue to be addressed for this particular structure is that the THz radiation re-emitted from the TTWWG output in free-space is not entirely collectable via conventional optical components, due to the sub-λ output end. Indeed, the output gap gout can be regarded as a dipole THz source irradiating the THz wave

across an extremely large radiation pattern (see Figure 2). Since the THz wave vector satisfies the condition $k_{THz}g_{out} = 2\pi g_{out}/\lambda_{THz} < 1$, Bethe's law of diffraction should to be applied to this case.[54] More in detail, in the Bethe's diffraction regime, the confocal parameter z_B (defined as the distance at which the beam spot area doubles) is inversely proportional to the second power of the wavelength, that is:

$$z_B = \frac{k_{THz}^2 g_{out}^3}{2} = \frac{4\pi^2 g_{out}^3}{\lambda_{THz}^2} \quad (6)$$

By inserting all values in Equation 6, we evaluated z_B = 0.76 μm at 1 THz, which would result in an excessive broadening of the THz beam diameter (> 10 cm) right after a few millimeters of propagation from the TTWWG output end. Therefore, the beam spot would be much larger than the clear aperture of many parabolic mirrors commonly employed in THz-TDS systems, which could only collect a fraction of the emitted THz beam. Such a strong beam diffraction would hamper the complete gathering of all the frequency components contained in re-mitted THz pulse spectrum.[40,55] In turn, this effect would alter the electric field waveform associated to the time-integrated THz pulse coupled out the TTWWG, especially at low frequencies (shorter z_B). In light of this observation, THz detection via either electro-optic sampling[56] or photoconductive switches[57], carried out in the far-field region, would lead to an incorrect reconstruction of the THz pulse shape, thus preventing us from correctly assessing the TTWWG integration functionality. In order to overcome the issue related to the unpractical sub-λ out-coupling, we recorded the THz waveform by implementing a detection method closely resembling the air-biased coherent detection (ABCD) technique,[55,58] directly within the TTWWG. Briefly, ABCD relies on the nonlinear interaction between the THz and an optical probe beam occurring in air, which generates a new beam at roughly the second harmonic (SH) of the probe beam.[59] If the THz-probe interaction region is biased with an external electric field (E_{bias}), the nonlinear mixing gives rise to a total SH intensity (I_{SH}) comprising a term linearly proportional to the THz electric field. By exploiting a heterodyne scheme,[58] this term

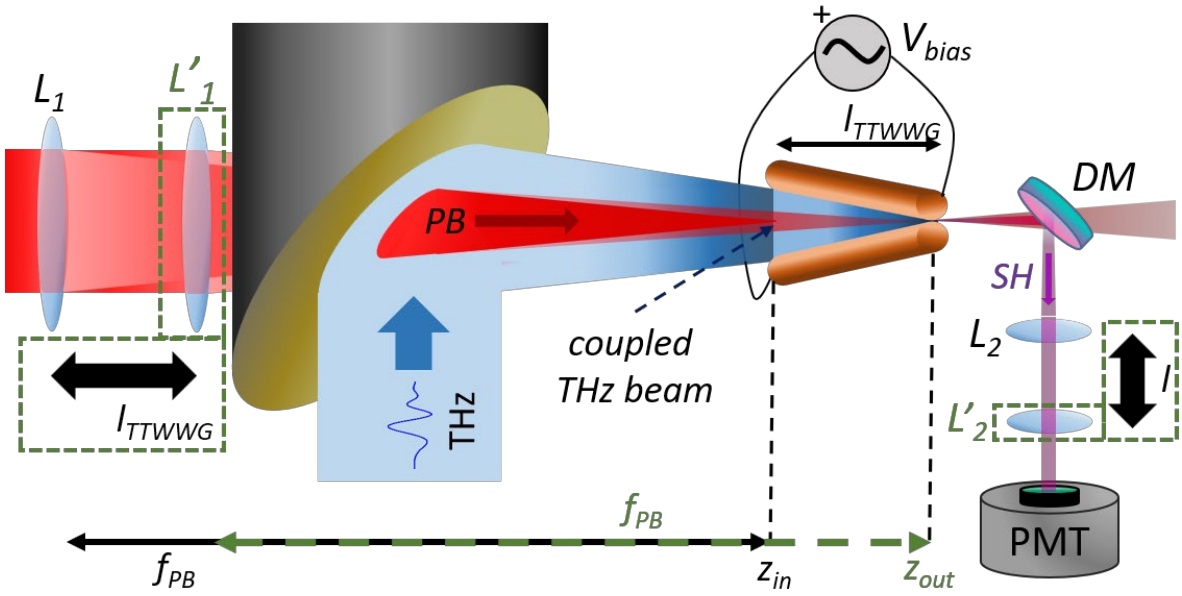

Figure 3. Sketch of the detection stage employed to record the THz waveforms. The TTWWG input is placed at the focal point of a 2-inch 90° off-axis mirror. The probe beam travels through a hole realized in the center of the parabolic mirror and then collinearly propagates with the THz beam inside the waveguide. Its focal point can be shifted along the z-axis by longitudinally translating lens L1. The emerging SH beam, resulting from the THz-probe interaction occurring inside the TTWWG biased at V_{bias}, is firstly separated from the remaining probe power by means of a dichroic mirror (DM) and then collected by lens L2. A photomultiplier tube (PMT) acquires the SH intensity. In order to retrieve the input THz pulse waveform, two tip-shaped metal pads replaced the TTWWG to perform conventional ABCD technique right at the mirror focal point.

can be extracted, leading to:

$$I_{SH}(t) \propto I_{PB}^2 E_{bias} E_{THz}(t) \tag{7}$$

where I_{PB} is the probe beam intensity. Equation 7 enables the reconstruction of both amplitude and phase of the THz pulse, by easily acquiring the SH intensity via an optical detector. We adapted the ABCD technique to the case of our TTWWG, as sketched in **Figure 3**, which shows the THz detection path of the experimental setup. The THz beam was focused into the waveguide by means of a 2-inch 90° parabolic mirror, whereas the probe beam was injected into the TTWWG from its input, thus propagating collinearly with the THz beam. The copper wires sustaining the propagation of the THz mode also played the role of metal contacts, allowing us to electrically bias the air region within the TWWG gap. The focal point of the probe beam was moved from the input position (L1) to the TTWWG output (L'1), by longitudinally translating the corresponding focusing lens position. The out-coming SH beam

was gathered by accordingly adjusting the position of the lens L2 (↔L'2). Finally, a photomultiplier tube (PMT) acquired the SH beam intensity as a function of the probe-THz time delay, converting it into an electric readout signal, recorded via lock-in detection. In the Supporting Information, we show that this approach is particularly suitable to locally reconstruct the THz electric field inside the TTWWG, since the SH intensity resembles the shape of the THz pulse that overlaps the probe beam at its focal point both temporally and spatially.[60]

4. Experimental and simulation results

We carried out the experimental investigation in two THz spectral regimes, namely broadband and ultra-broadband.[5] In both cases, the experiments implied the use of a 150 fs, 1 kHz, 2 mJ, 800 nm Ti:Sapphire pulsed laser, which was split into the pump and probe beam arms. While the probe beam was fixed at a power value of 35 mW and focused via a 20-cm-lens into the waveguide to implement the THz field detection scheme, the pump beam was used to feed either a lithium niobate (LN)-based THz source[61] (broadband) or a two-color plasma THz source[32] (ultra-broadband). Experiments were performed under standard air humidity conditions. We specifically used these two types of sources because of their different THz spectral emission. On the one hand, the LN source provides a THz pulse train with a ~2.7-THz-wide spectrum and a relatively low central frequency (< 1 THz). This type of source indeed represents the perfect tool to test the time integration functionality of the TTWWG. On the other hand, the ultrashort THz pulses emitted by the plasma source cover spectra as wide as the entire THz range, thus allowing for a complete study of the TTWWG spectral response, including THz wavelengths as short as the output gap size (~30 μm). In addition, the shape of the THz pulse is different in the two cases, thus allowing us to demonstrate that the time-domain integration is independent of the input THz pulse. We also carried out Finite-Difference Time-Domain (FDTD) simulations in order to support our experimental investigations, and to predict

the TTWWG behavior in terms of the coupled and propagating THz pulse. For each source, we retrieved the THz waveform at the TTWWG output (E_{out}). The input pulse (E_{in}) was evaluated via a second set of simulations performed by excluding the waveguide from the calculation domain and by letting the pulse propagate into free space. In order to confirm time domain integration, we numerically calculated the first-order time derivative of E_{out} (i.e., dE_{out}/dt) and compared it with the Ein waveform. The same procedure was applied to the experimental waveforms. The reason behind this strategy stems from the fact that differentiating the output signal, rather than integrating the input pulse, has the advantage of minimizing the effects of numerical artefacts, e.g., the superposition of a spurious offset value in the integral waveform. Such artefacts could lead to alterations of the THz pulse shape. We recall that, by definition, propagating electromagnetic transients have a zero-mean value.[62] Finally, in order to quantify the correctness of the time integration, and in turn of the overall TTWWG performance, we evaluated the root mean squared error (RMSE) between the input and time derivative of the output waveforms, for both simulations ($RMSE_{sim}$) and experiments ($RMSE_{exp}$).[63] More details about the calculus of the RMSE are given in the Supporting Information. Here, we highlight that in the ideal case, i.e., when two waveforms have the same exact shape, the RMSE parameter is identically equal to zero, while it increases as the agreement between two curves worsens.

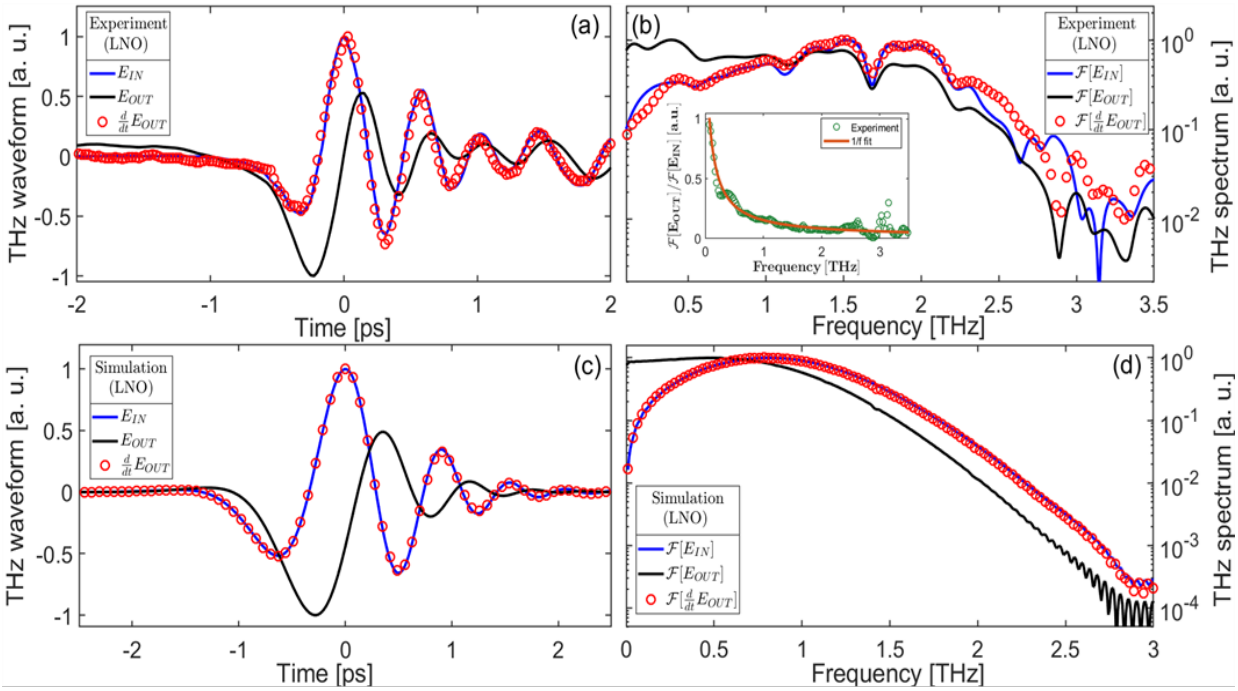

Figure 4. Experimental (a)-(b) and simulated (c)-(d) temporal and spectral curves retrieved by employing an LN THz source. In all panels, the blue solid line, black solid line and red open circles, indicate the input signal, the output signal and its numerical first-time derivative, respectively. Both temporal and spectral curves are normalized with respect to their own maxima. In the legend of (b) and (d), F stands for the Fourier Transform of their corresponding temporal waveforms. The inset in (b) shows the experimental spectral response of the TTWWG (open green circles) evaluated as in Eq. (3), fitted with a *1/f*-curve (orange solid line).

4.1. Broadband regime

The setup configuration adopted for the generation of THz pulses via optical rectification in a 63°-cut LN crystal, consisted of a conventional tilt-pulse-front scheme,[61] as depicted in Figure S5 in the Supporting Information. While the TTWWG waveforms were recorded as previously discussed we carried out the standard ABCD technique in free space for the acquisition of the input waveform. To do so, we used two metallic tips separated by a 1.1-mm-wide air gap (the same value of $2g_{in}$) and biased with a 2-kV-square wave voltage (at 500 Hz), while the probe beam was focused to the initial position of lens L1. The temporal curves recorded for this source are displayed in **Figure 4**a, whereas their corresponding spectra, evaluated via a Fast Fourier Transform (FFT) algorithm are presented in Figure 4b. We can easily recognize the significant difference between the E_{in} and E_{out} curves, as underlined by the different temporal evolution of

the electric field cycles associated to the two temporal transients. Moreover, the spectrum of the output waveform shows a considerable enhancement of the low frequency components by almost one order of magnitude, with respect to the input pulse. This is accompanied by a noticeable shift of the peak frequency towards lower values. Finally, the inset in Figure 4b depicts the ratio between the two spectra $E_{out}(f)$ and $E_{in}(f)$, which represents the experimental spectral transfer function of the TTWWG, as defined in Equation 3. This curve unveils a good match with the *1/f*-response featuring an ideal time integrator device. In order to further confirm a proper correctness of the time integration of the THz pulse, we show the curve corresponding to the numerically evaluated time derivative of E_{out} in the same plot. The very good agreement between the dE_{out}/dt curve and that of the input Ein in the time domain is validated by an $RMSE_{exp}$ as low as 2.4%. Finally, Figure 4b indicates that the time integration was achieved over a THz spectral window larger than 2 THz. Numerical results shown in Figure 4c and 4d, additionally support our findings, as the simulated curves well reproduce the experimental transients, at the same time revealing a good matching between E_{in} and dE_{out}/dt in both time and spectral domains. For the temporal waveforms, the calculated $RMSE_{sim}$ is 1.7%, fairly close to the experimental value.

4.2. Ultra-broadband regime

The two-color THz plasma source was implemented by focusing together the pump beam with its second harmonic, achieved through a 100-μm-thick BBO crystal placed in the focusing path of a 4'' parabolic mirror (see Figure S6 in the Supporting Information).[64] As for the previous case, **Figure 5**a depicts the experimental temporal waveforms recorded at the TTWWG input (E_{in}) and output (E_{out}), whereas Figure 5b shows their corresponding spectra. We note that the TTWWG spectrum is once again strongly enhanced in the low frequency range, as stated by the ~1-THz-red shift experienced by the peak frequency, compared to the air case. Remarkably, even though in this case the value gout can no longer be considered perfectly sub-λ in the

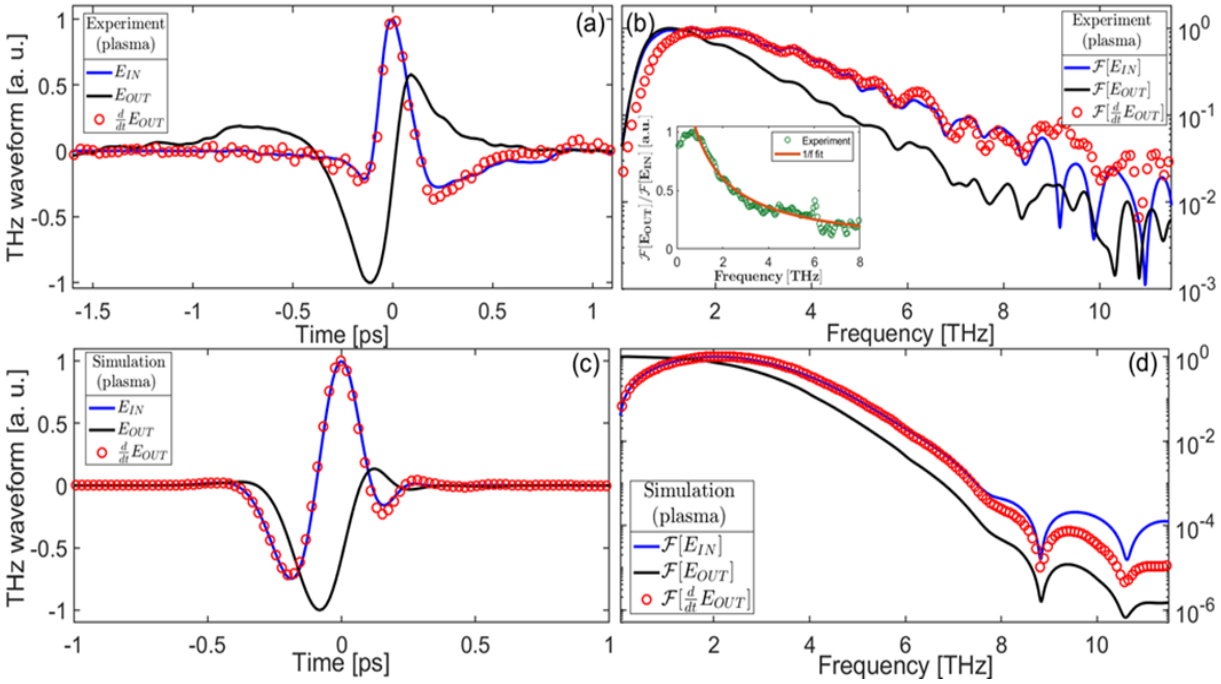

Figure 5. Experimental (a)-(b) and simulated (c)-(d) temporal and spectral curves retrieved by employing a two-color plasma THz source. In all panels, the blue solid line, black solid line and red open circles, indicate the input signal, the output signal and its numerical first-time derivative, respectively. Both temporal and spectral curves are normalized with respect to their own maxima. In the legend of (b) and (d), *F* stands for the Fourier Transform of their corresponding temporal waveforms. The inset in (b) shows the experimental transfer function (green open circles) of the TTWWG evaluated according to Eq. (3) along with a *1/f*-fitting curve (orange solid line).

highest part of the spectrum, the numerical time derivative of the output waveform, dE_{out}/dt, shows a fairly good agreement with the input transient. This is also confirmed by the reasonably good overlap between the input spectrum and the one corresponding to the dE_{out}/dt curve, which, as expected, begins to worsen beyond 8 THz. The small inconsistency observed at relatively low frequencies (< 1 THz) may be ascribed to two main effects due to the plasma source characteristics. First, since we kept the same focusing geometry at the detection stage, the larger spectrum featuring this type of THz pulses resulted in a smaller focal spot ($1/e^2$-intensity diameter of ~150 μm) at the input of the TTWWG, compared to the LN source (~1 mm). Moreover, THz beams generated by a plasma filament typically exhibit a ring-shaped profile in the far field, which, differently from a Gaussian profile, is subsequently focused down to a cross-like shape.[65] These two concomitant effects may worsen the in-coupling efficiency at

lower frequencies. The evaluated $RMSE_{exp}$ is around 12.4%. Finally, the inset in Figure 5b shows that the TTWWG transfer function follows quite closely the ideal *1/f*-curve over a spectral window as large as ~8 THz. Simulation results, computed by accounting for the smaller THz beam spot at the TTWWG input gap, reproduce the experimental trends with good agreement, as shown in Figure 5c and 5d. In particular, in Figure 5d, the spectrum of the TTWWG pulse shows an enhancement of the low frequency components, and a corresponding red shift of the peak frequency, compared to the input case. Moreover, simulations confirm the 8-THz-wide operational spectral range, experimentally observed for this TTWWG geometrical configuration. Finally, in the simulations $RMSE_{sim}$ is around 9%, approaching the value found in the experiments. As a final remark, it is worth mentioning that a better time integration of such an ultra-broadband THz signal could be easily achieved by reducing the output gape size, gout, and accordingly adjusting the input aperture angle of the TTWWG.

5. Conclusions

In conclusion, we demonstrated time-domain integration of broadband, and, potentially, ultra-broadband THz pulses. This has been achieved by exploiting the frequency response of a tapered two-wire waveguide, featuring a wire gap that shrinks down to a sub-wavelength size while moving from the input to the output end. The particularly tight confinement of the THz radiation induced by such a reduced output gap size, results in the enhancement of the propagating electric field, which is inversely proportional to the THz frequency. Such a behavior resembles the typical spectral transfer function of a conventional time integrator device. Such functionality has been proved by comparing the THz waveforms acquired in air (i.e., the input pulse) and right at the TTWWG output gap (i.e., the time-integrated pulse). In particular, the TTWWG waveforms have been acquired by carrying out a local field-resolved detection technique, based on the ABCD mechanism, in order to minimize alterations of the shape of the time-integrated THz transients. Our prototype device has the potential to become

a key building block for the construction of a wide range of complex analog systems for signal-processing and computing applications based on THz waves. Among those, we can mention real-time computation of differential equations and digital counting.[48,66] To give a more concrete example, we envision that the prototype integrator device demonstrated here may be employed for the implementation of emphasis/de-emphasis communication protocols, similar to those used in conventional RF systems. This application would involve a pre-conditioning (*emphasis*) of the THz pulses before being delivered in free space and detected in a THz receiver, where the time integration (*de-emphasis*) is used to restore the original information signal. Through this strategy, the higher frequencies are first enhanced to counteract the atmospheric absorption loss (particularly strong in the THz range) and subsequently attenuated by the integration action so as to equalize the signal to its original shape. This may enable an increase in the propagation distances of long-haul communication links using THz radiation, a critical advancement in these systems.

6. Methods

TTWWG-based THz electric field detection: In order to directly monitor the THz waveform propagating along the TTWWG, we implemented a local field-resolved detection method, which consists in a revised version of the air-biased coherent detection (ABCD) technique. As mentioned in the Section 3, the mechanism underlying the detection process is governed by Equation 7, which states that the readout signal I_{SH} is linearly proportional to the bias (E_{bias}) and THz (E_{THz}) electric fields, while it shows a quadratic dependence on the probe intensity I_{PB}. As such, we expect that the contribution to the total SH intensity would only arise from a restricted region across the probe focal plane. In order to confirm this assumption, we analytically evaluated Equation 7 for the specific case of our TTWWG geometry and the experimental conditions employed in this study. Specifically, we included the probe beam intensity (I_{PB}), as well as the bias and THz electric fields dependence on the propagation coordinate z.

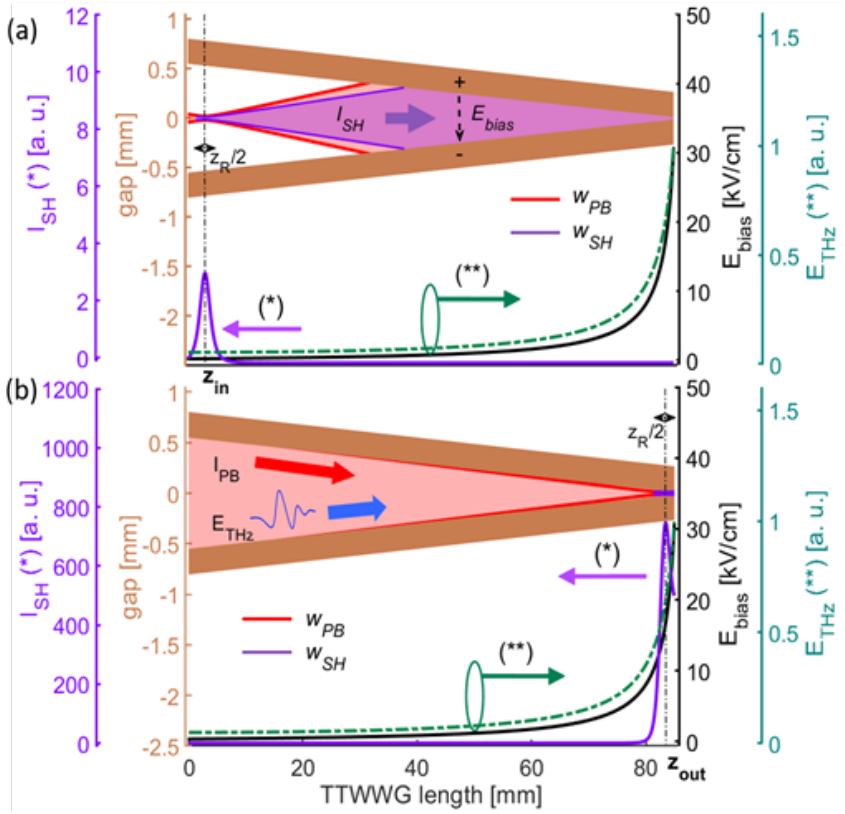

Figure 6. Mechanism of the TTWWG-integrated THz detection method giving rise to the ISH signal, for the case of a probe beam focused at the waveguide (a) input (z_{in} = 3 mm) and (b) output (z_{out} = 83 mm). In both plots, THz, probe and SH beams propagate from left to right and are polarized along the vertical axis (i.e., the plane containing the two wires). For the sake of clarity, we also report the trends of the bias and THz electric fields along the whole TTWWG. The contributions to the total SH beam are mainly generated in a region as wide as $z_R/2$.

By considering the waveguide parameters indicated in Figure 2, the analytical expressions for the first two terms in the right-hand side of Equation 7 are determined as:

$$I_{PB}(z) = \frac{I_0}{\sqrt{1+\left(\frac{z-z_f}{z_R}\right)^2}} \tag{8}$$

$$E_{bias}(z) = \frac{V_{bias}}{\sqrt{d^2(z)-R^2}\cosh^{-1}\left(\frac{d(z)}{R}\right)} \tag{9}$$

In Equation 8, $z_R = \pi(w_{PB})^2\lambda^{-1}_{PB}$ = 1.6 mm is the probe Rayleigh length, where w_{PB} = 20 μm is the waist size and λ_{PB} = 800 nm is the wavelength of the probe beam, V_{bias} is the voltage applied to the wires, while I_0 is its peak intensity, exhibited at the focal point z_f. From Equation 9, we determined that a bias electric field of E_{bias} ~ 31 kVcm^{-1} (close to the air dielectric strength) is

established between the two wires at $z = l_{TTWWG}$ (i.e., the output gap), when the applied on the propagation coordinate z. By considering the waveguide parameters indicated in Figure 2, the analytical expressions for the first two terms in the right-hand side of Equation 7 are determined as: voltage is V_{bias} = 150 V. Since an analytical expression for the THz electric field along the waveguide is not easily accessible, we used the data of the FDTD simulations to infer the evolution of a test THz pulse propagating inside the TTWWG. In particular, we considered a pulse centered at f_c = 0.8 THz, with bandwidth of B_w = 4 THz. We also considered the case of a Gaussian beam focused onto the TTWWG input, so as to consider the in-coupling effect in the calculation. For the purpose of this study, we simply retrieved the absolute peak values exhibited by the THz electric field along the z-axis, in between the wires. The result of the complete calculation is presented in **Figure 6**, where we show the case of a probe beam focused close to either (a) the waveguide input (z_f = 3 mm inside the TTWWG) or (b) its output (z_f = 83 mm) via a 20-cm-lens. We note that, while both the THz and bias electric fields monotonically augment as a function of the TTWWG length, with a steep increase near the output gap, the THz-induced SH intensity is significant only around a fraction of the probe Rayleigh length, being negligible outside this region. This essentially holds for any position of the probe focal point along the z-axis, as highlighted in Figure 6b, where the probe beam is focused into the TTWWG output, yet with an SH peak amplitude two orders of magnitude higher than for the case in Figure 6a. This observation ensures that the proposed method allows for the retrieval of the THz waveform in a region as short as half of the probe Rayleigh length (~$z_R/2$). Furthermore, when the probe beam is focused exactly at the output gap ($z = l_{TTWWG}$), the interaction region can be considered as short as $z_R/4$ only, since the THz strength drops immediately outside the waveguide and does no longer contribute to SH generation.

Supporting Information

Supporting Information is available from the Wiley Online Library or from the author.

Acknowledgements

G.B. and A.T. contributed equally to this work. This work (for R.M. and J.A.) was supported by the Natural Sciences and Engineering Research Council of Canada (NSERC) through the Discovery and Strategic grant programs, by the Ministère de l'Économie, de la Science et de l'Innovation (MESI) of Québec and by PRIMA Quebec. J.D. acknowledges the financial support from Mitacs Elevate Postdoctoral Fellowship. We also acknowledge support from our industrial partners ACME Engineering Prod. Ltd., TeTechS Inc., Integrity Testing Inc., Lumenera Corporation, 1Qbit, and Newlight Photonics. R.M. is affiliated to IFFS as an adjoint faculty.

Received: ((will be filled in by the editorial staff))
Revised: ((will be filled in by the editorial staff))
Published online: ((will be filled in by the editorial staff))

References

[1] M. Tonouchi, *Nat. Photonics* **2007**, *1*, 97.

[2] B. Ferguson, and X.-C. Zhang, *Nat. Mater.* **2002**, *1*, 26.

[3] N. Horiuchi, *Nat. Photonics* **2010**, *4*, 140.

[4] H. W. Hübers, *Nat. Photonics* **2010**, *4*, 503.

[5] Y. S. Lee, *Principles of Terahertz Science and Technology*, Springer, **2009**.

[6] A. Tomasino, A. Parisi, S. Stivala, P. Livreri, A. C. Cino, A. C. Busacca, M. Peccianti, and R. Morandotti, *Sci. Rep.* **2013**, *3*.

[7] D. M. Mittleman, R. H. Jacobsen, R. Neelamani, R. G. Baraniuk, and M. C. Nuss, *Appl. Phys. B Lasers Opt.* **1998**, *67*, 379.

[8] C. Zandonella, *Nature* **2003**, *424*, 721.

[9] J. Dong, H. Breitenborn, R. Piccoli, L. V Besteiro, P. You, D. Caraffini, Z. M. Wang, A. O. Govorov, R. Naccache, F. Vetrone, L. Razzari, and R. Morandotti, *Biomed. Opt. Express* **2020**, *11*, 2254.

[10] H. Breitenborn, J. Dong, R. Piccoli, A. Bruhacs, L. V. Besteiro, A. Skripka, Z. M. Wang, A. O. Govorov, L. Razzari, F. Vetrone, R. Naccache, and R. Morandotti, *APL Photonics* **2019**, *4*, 126106.

[11] W. Withayachumnankul, and D. Abbott, *Nat. Photonics* **8**, 593–594 (2014).

[12] D. M. Mittleman, *Opt. Express* **2018**, *26*, 9417.

[13] F. Rutz, M. Koch, S. Khare, M. Moneke, H. Richter, and U. Ewert, *Int. J. Infrared Millimeter Waves* **2006**, *27*, 547.

[14] K. Lien Nguyen, T. Friščić, G. M. Day, L. F. Gladden, and W. Jones, *Nat. Mater.* **2007**, *6*, 206.

[15] T. Nagatsuma, G. Ducournau, and C. C. Renaud, *Nat. Photonics* **2016**, *10*, 371.

[16] S. Ummethala, T. Harter, K. Koehnle, Z. Li, S. Muehlbrandt, Y. Kutuvantavida, J. Kemal, P. Marin-Palomo, J. Schaefer, A. Tessmann, S. K. Garlapati, A. Bacher, L. Hahn, M. Walther, T. Zwick, S. Randel, W. Freude, and C. Koos, *Nat. Photonics* **13**, 519–524 (2019).

[17] H. J. Song, and T. Nagatsuma, *IEEE Trans. Terahertz Sci. Technol.* **1**, 256–263 (2011).

[18] A. J. Seeds, H. Shams, M. J. Fice, and C. C. Renaud, *J. Light. Technol.* **2015**, *33*, 579.

[19] J. Federici, and L. Moeller, *J. Appl. Phys.* **107**, (2010).

[20] S. F. Busch, S. Schumann, C. Jansen, M. Scheller, M. Koch, and B. M. Fischer, *Appl. Phys. Lett.* **2012**, *100*, 261109.

[21] R. Mendis, A. Nag, F. Chen, and D. M. Mittleman, *Appl. Phys. Lett.* **2010**, *97*, 131106.

[22] M. K. Mridha, A. Mazhorova, M. Clerici, I. Al-Naib, M. Daneau, X. Ropagnol, M. Peccianti, C. Reimer, M. Ferrera, L. Razzari, F. Vidal, and R. Morandotti, *Opt. Express* **2014**, *22*, 22340.

[23] J. Xie, X. Zhu, H. Zhang, X. Zang, L. Chen, A. V. Balakin, A. P. Shkurinov, and Y. Zhu, *Opt. Express* **2020**, *28*, 7898.

[24] M. Daniel, *Nature* **444**, 560–561 (2006).

[25] N. Karl, K. Reichel, H. T. Chen, A. J. Taylor, I. Brener, A. Benz, J. L. Reno, R. Mendis, and D. M. Mittleman, *Appl. Phys. Lett.* **2014**, *104*, 091115.

[26] K. S. Reichel, N. Lozada-Smith, I. D. Joshipura, J. Ma, R. Shrestha, R. Mendis, M. D. Dickey, and D. M. Mittleman, *Nat. Commun.* **2018**, *9*, 1.

[27] T. Yasui, H. Takahashi, K. Kawamoto, Y. Iwamoto, K. Arai, T. Araki, H. Inaba, and K.

Minoshima, *Opt. Express* **2011**, *19*, 4428.

[28] M. Katoh, and S. Bielawski, *Nat. Photonics* **2012**, *6*, 76.

[29] A. Rice, Y. Jin, X. F. Ma, X. C. Zhang, D. Bliss, J. Larkin, and M. Alexander, *Appl. Phys. Lett.* **1994**, *64*, 1324.

[30] M. Tani, S. Matsuura, K. Sakai, and S. Nakashima, *Appl. Opt.* **1997**, *36*, 7853.

[31] D. J. Cook, and R. M. Hochstrasser, *Opt. Lett.* **2000**, *25*, 1210.

[32] M. Clerici, M. Peccianti, B. E. Schmidt, L. Caspani, M. Shalaby, M. Giguère, A. Lotti, A. Couairon, F. Légaré, T. Ozaki, D. Faccio, and R. Morandotti, *Phys. Rev. Lett.* **2013**, *110*.

[33] N. K. Berger, B. Levit, B. Fischer, M. Kulishov, D. V. Plant, and J. Azaña, *Opt. Express* **2007**, *15*, 371.

[34] M. Kulishov, and J. Azaña, *Opt. Express* **2007**, *15*, 6152.

[35] C. Cuadrado-Laborde, and M. V. Andrés, *Opt. Lett.* **2009**, *34*, 833.

[36] M. A. Preciado, and M. A. Muriel, *Opt. Lett.* **2008**, *33*, 1348.

[37] A. Filin, M. Stowe, and R. Kersting, *Opt. Lett.* **2001**, *26*, 2008.

[38] F. Amirkhan, A. Robichaud, X. Ropagnol, M. Gratuze, T. Ozaki, F. Nabki, and F. Blanchard, *Opt. Lett.* **2020**, *45*, 3589.

[39] R. Mendis, and D. Grischkowsky, *Opt. Lett.* **2001**, *26*, 846.

[40] K. Iwaszczuk, A. Andryieuski, A. Lavrinenko, X.-C. Zhang, and P. U. Jepsen, *Appl. Phys. Lett.* **2011**, *99*, 071113.

[41] M. Mbonye, R. Mendis, and D. M. Mittleman, *Appl. Phys. Lett.* **2009**, *95*, 233506.

[42] R. E. Collin, *Foundations for Microwave Engineering*, IEEE Press, **2001**.

[43] S. Ramo, J. R. Whinnery, and T. Van Duzer, *Fields and Waves in Communication Electronics*, Wiley, **1994**.

[44] G. Yan, A. Markov, Y. Chinifooroshan, S. M. Tripathi, W. J. Bock, and M. Skorobogatiy, *Opt. Lett.* **2013**, *38*, 3089.

[45] E. S. Lee, and T.-I. Jeon, *Opt. Express* **2012**, *20*, 29605.

[46] E. S. Lee, S.-G. Lee, C.-S. Kee, and T.-I. Jeon, *Opt. Express* **2011**, *19*, 14852.

[47] S. Haykin, and M. Michael, *An Introduction to Analog and Digital Communications*, Wiley, **2006**.

[48] J. Azaña, *IEEE Photonics J.* **2**, 359–386 (2010).

[49] M. Ferrera, Y. Park, L. Razzari, B. E. Little, S. T. Chu, R. Morandotti, D. J. Moss, and J. Azaña, *Nat. Commun.* **2010**, *1*, 1.

[50] J.-H. Kang, D.-S. Kim, and M. Seo, **2018**, *7*, 763.

[51] M. A. Seo, H. R. Park, S. M. Koo, D. J. Park, J. H. Kang, O. K. Suwal, S. S. Choi, P. C. M. Planken, G. S. Park, N. K. Park, Q. H. Park, and D. S. Kim, *Nat. Photonics* **2009**, *3*, 152.

[52] A. Tomasino, R. Piccoli, Y. Jestin, S. Delprat, M. Chaker, M. Peccianti, M. Clerici, A. Busacca, L. Razzari, and R. Morandotti, *APL Photonics* **2018**, *3*, 110805.

[53] H. Pahlevaninezhad, T. E. Darcie, and B. Heshmat, *Opt. Express* **2010**, *18*, 7415.

[54] H. A. Bethe, *Phys. Rev.* **1944**, *66*, 163.

[55] K. Iwaszczuk, A. Andryieuski, A. Lavrinenko, X.-C. Zhang, and P. U. Jepsen, *Opt. Express* **2012**, *20*, 8344.

[56] Q. Wu, and X. C. Zhang, *Appl. Phys. Lett.* **1995**, *67*, 3523.

[57] Y. C. Shen, P. C. Upadhya, H. E. Beere, E. H. Linfield, A. G. Davies, I. S. Gregory, C. Baker, W. R. Tribe, and M. J. Evans, *Appl. Phys. Lett.* **2004**, *85*, 164.

[58] N. Karpowicz, J. Dai, X. Lu, Y. Chen, M. Yamaguchi, H. Zhao, X. C. Zhang, L. Zhang, C. Zhang, M. Price-Gallagher, C. Fletcher, O. Mamer, A. Lesimple, and K. Johnson, *Appl. Phys. Lett.* **2008**, *92*, 011131.

[59] A. Nahata, and T. F. Heinz, *Opt. Lett.* **1998**, *23*, 67.

[60] J. Liu, J. D. J. Dai, S. L. C. S. L. Chin, and X.-C. Zhang, *Lasers Electro-Optics Quantum Electron. Laser Sci. Conf. (QELS), 2010 Conf.* **2010**, *4*, 627.

[61] J. Hebling, A. G. Stepanov, G. Almási, B. Bartal, and J. Kuhl, *Appl. Phys. B Lasers Opt.* **2004**, *78*, 593.

[62] J.-C. Diels, and W. Rudolph, *Ultrashort Laser Pulse Phenomena : Fundamentals, Techniques, and Applications on a Femtosecond Time Scale*, Elsevier/Academic Press, **2006**.

[63] F. M. Dekking, C. Kraaikamp, H. P. Lopuhaä, and L. E. Meester, *A Modern Introduction to Probability and Statistics*, Springer London, London, **2005**.

[64] A. Tomasino, A. Mazhorova, M. Clerici, M. Peccianti, S.-P. Ho, Y. Jestin, A. Pasquazi, A. Markov, X. Jin, R. Piccoli, S. Delprat, M. Chaker, A. Busacca, J. Ali, L. Razzari, and R. Morandotti, **2017**, *4*, 1358.

[65] P. Klarskov, A. C. Strikwerda, K. Iwaszczuk, and P. U. Jepsen, *New J. Phys.* **2013**, *15*, 075012.

[66] R. Slavík, Y. Park, N. Ayotte, S. Doucet, T.-J. Ahn, S. LaRochelle, and J. Azaña, *Opt. Express* **2008**, *16*, 18202.

Giacomo Balistreri, Alessandro Tomasino, Junliang Dong, Aycan Yurtsever, Salvatore Stivala, José Azaña, Roberto Morandotti**

Time-domain integration of broadband terahertz pulses in a tapered two-wire waveguide

The ever-increasing demand for higher bandwidths in wireless communications systems and ultra-high speed signal processing operations, has pushed state-of-the-art technologies to operate at terahertz frequencies. Such new platforms urgently require the development of fundamental building blocks, enabling wideband performance. Here, we demonstrate a time-domain integrator device for broadband THz pulses, relying on a tapered two-wire waveguide.